



Article

Analyzing the Effects of Multi-Layered Porous Intraluminal Thrombus on Oxygen Flow in Abdominal Aortic Aneurysms

Alexis Throop 1, Durwash Badr 1, Michael Durka 2, Martina Bukač 3 and Rana Zakerzadeh 1,* 10

- Department of Engineering, Rangos School of Health Sciences, Duquesne University, Pittsburgh, PA 15282, USA
- Department of Mechanical Engineering & Material Sciences, University of Pittsburgh, Pittsburgh, PA 15260, USA
- Department of Applied and Computational Mathematics and Statistics, University of Notre Dame, Notre Dame, IN 46556, USA
- * Correspondence: zakerzadehr@duq.edu

Abstract: Determination of abdominal aortic aneurysm (AAA) rupture risk involves the accurate prediction of mechanical stresses acting on the arterial tissue, as well as the wall strength which has a correlation with oxygen supply within the aneurysmal wall. Our laboratory has previously reported the significance of an intraluminal thrombus (ILT) presence and morphology on localized oxygen deprivation by assuming a uniform consistency of ILT. The aim of this work is to investigate the effects of ILT structural composition on oxygen flow by adopting a multilayered porous framework and comparing a two-layer ILT model with one-layer models. Three-dimensional idealized and patient-specific AAA geometries are generated. Numerical simulations of coupled fluid flow and oxygen transport between blood, arterial wall, and ILT are performed, and spatial variations of oxygen concentrations within the AAA are obtained. A parametric study is conducted, and ILT permeability and oxygen diffusivity parameters are individually varied within a physiological range. A gradient of permeability is also defined to represent the heterogenous structure of ILT. Results for oxygen measures as well as filtration velocities are obtained, and it is found that the presence of any ILT reduces and redistributes the concentrations in the aortic wall markedly. Moreover, it is found that the integration of a porous ILT significantly affects the oxygen transport in AAA and the concentrations are linked to ILT's permeability values. Regardless of the ILT stratification, maximum variation in wall oxygen concentrations is higher in models with lower permeability, while the concentrations are not sensitive to the value of the diffusion coefficient. Based on the observations, we infer that average one-layer parameters for ILT material characteristics can be used to reasonably estimate the wall oxygen concentrations in aneurysm models.

Keywords: abdominal aortic aneurysm (AAA); intraluminal thrombus (ILT); porous structure; patient-specific; computational fluid dynamics (CFD); parametric analysis



Citation: Throop, A.; Badr, D.;
Durka, M.; Bukač, M.; Zakerzadeh, R.
Analyzing the Effects of
Multi-Layered Porous Intraluminal
Thrombus on Oxygen Flow in
Abdominal Aortic Aneurysms.

Oxygen 2022, 2, 518–536.
https://doi.org/10.3390/
oxygen2040034

Academic Editor: John T. Hancock

Received: 20 September 2022 Accepted: 17 October 2022 Published: 24 October 2022

Publisher's Note: MDPI stays neutral with regard to jurisdictional claims in published maps and institutional affiliations.



Copyright: © 2022 by the authors. Licensee MDPI, Basel, Switzerland. This article is an open access article distributed under the terms and conditions of the Creative Commons Attribution (CC BY) license (https://creativecommons.org/licenses/by/4.0/).

1. Introduction

An abdominal aortic aneurysm (AAA) is a progressive and localized dilation of the infrarenal aorta that results from the degradation of the extracellular matrix in the arterial wall [1], which is often asymptomatic but fatal upon rupture [2]. The mortality of patients with ruptured AAA is 50–80% [3] and about half die before being admitted to the hospital [4]. Previous findings show that AAA-related death has been the 12th–15th leading cause of death in the USA, UK, and several European countries [4–6]. In particular, acute AAA ruptures are estimated to cause 4% to 5% of sudden death in developed countries and are ranked as the 14th leading cause of death in the United States [7]. The prevalence of AAA in general population ranges from 1.0% to 14.2% in men and 0.2% to 6.4% in women [8].

The rupture of AAA is facilitated by the structural degradation of the arterial wall until the mechanical stress acting on the wall exceeds the strength of the tissue and generally occurs jointly with the formation of an intraluminal thrombus (ILT) in the AAA bulge. The ILT is present in approximately 75% of AAAs [9].

ILTs are composed of fibrin, blood proteins, blood cells, platelets, and cellular debris [10]. Their complex structure is traversed from the luminal to the abluminal surface by a continuous network of interconnected canaliculi [11]. ILT has been shown to be a non-homogeneous material, with two major types: "continuous" and "discrete" transitions [10,12]. A continuous ILT is homogeneous and uniform, associated with gradual transmural changes in structural mechanics with strong radial connectivity; while a discrete ILT is differentiated into three layers: luminal, medial, and abluminal [13]. The luminal layer is considered as nearest to the blood, followed by the medial, and the abluminal is nearest to the aneurysm wall [7]. Characteristic properties are generally distinct among these three primary layers. Each layer of discrete ILT varies in color: the luminal appears red because of the greater proportion of erythrocytes. The medial (white to yellow) and abluminal (dark yellow to brown) layers are acellular and have greater density toward the abluminal side [14,15]. It should be noted that not all ILTs contain all three layers. Specifically, the medial and abluminal layers have similar microstructural features and are commonly considered as one uniform layer [16]. Figure 1b shows an ILT, removed intact from a large AAA, with visible characteristic layers of discrete thrombus. In particular, two distinct layers are found within most ILT, as reported by [16,17].

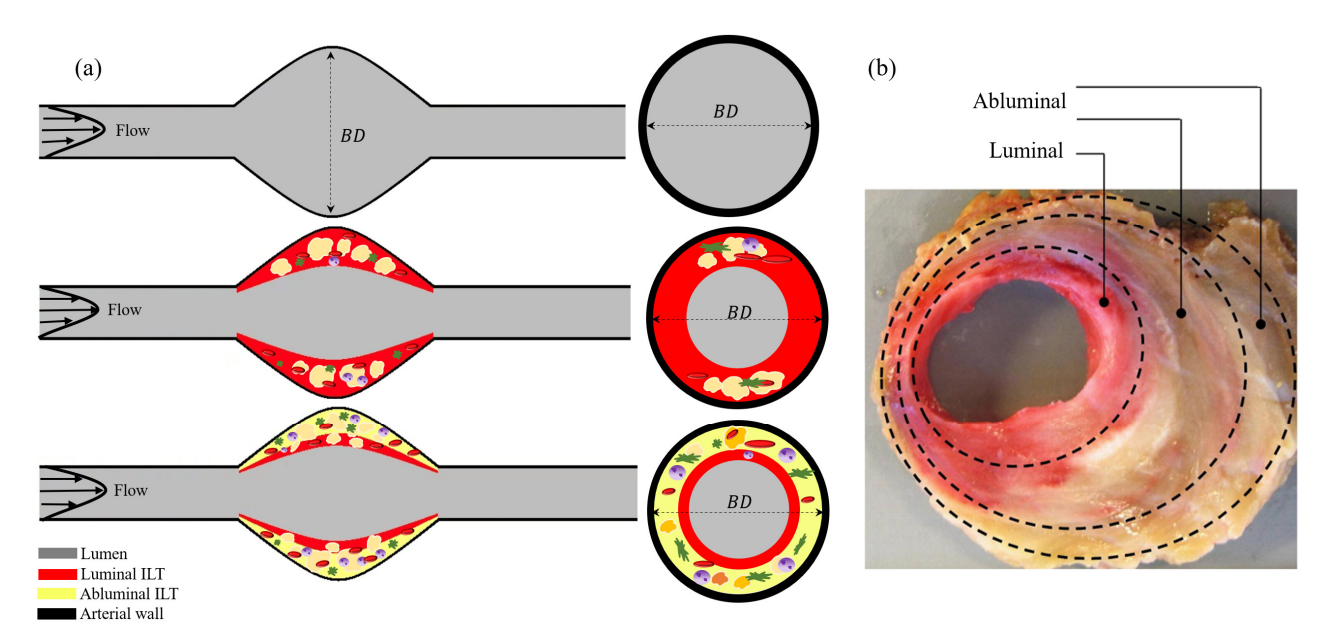


Figure 1. (a) A schematic of three-dimensional, axially symmetric AAA geometries used in this study is shown, including a model which lacks an ILT, a model containing a homogeneous ILT layer, and a model with a multi-layered ILT demonstrating its heterogeneity. In the two-layer ILT models, the abluminal layer and luminal layer thickness are two-thirds and one-third, respectively. *BD* represents the bulge diameter of the aneurysm. (b) Cross-section of the bulk ILT tissue harvested from elective human AAA repair, where luminal and abluminal layers are indicated; adapted with permission from [18], Elsevier, 2022.

The role of ILT in AAA rupture is unclear. Diverse findings from the literature regarding the role of ILT in AAA progression are discussed by Wilson et al. [13], which have shown that ILT provides a biomechanical advantage by decreasing wall stresses but contributes to oxygen deprivation in the arterial wall and decreases its strength. Qualitative information is obtained on how ILT presence influences mechanical stresses in AAA models by a few earlier investigations [19–24]. These studies have found that from a mechanical

vantage, ILT can act as a structural enhancement; thus, reducing the risk of aneurysm rupture by bearing some of the arterial mechanical load. However, it is known that ILT presence influences localized transluminal oxygen flow, which can trigger angiogenesis and aggravate inflammatory response in the aneurysmal wall [25].

To maintain the health of the arterial wall, sufficient transluminal oxygen transport is essential. Several prior studies have demonstrated the "hypoxia-mediated wall weakening" and hypothesized that ILTs can play a key role in directly influencing collagen and elastin production and decreasing arterial wall strength [26,27]. The deposition of ILT leads to a relatively hypoxic environment with increased proteolytic activity in the aortic wall nearest to the thick ILTs [26]. Under normal circumstances, aortic wall oxygenation reaches media and adventitia from the lumen, leaving less dependency on the nutrients provided by the vasa vasorum [28]. With increasing aortic wall inflammation, the vasa vasorum dilates to maintain the vessel integrity [29]. In support of the hypoxia theory, Vorp et al. [27] demonstrated that areas with thick ILT had lower oxygen pressure compared with those with thin ILT which resulted in greater inflammation, greater hypoxia-specific peptide, and decreased tensile strength. Therefore, the hypoxic environment in AAA may decrease the aortic wall structural integrity and lead to its eventual rupture (see a comprehensive review of investigations on the potential importance of hypoxia in [30]).

Mathematical models and numerical simulations have been demonstrated to show a high potential to generate and test competing hypotheses and pave the way for a more substantial research effort in vascular disease (recent progress in AAA computational modeling is reviewed in [31]). Although ILTs consist of layers with different material properties, earlier finite element analyses of AAAs have largely considered ILT to be homogeneous in mechanical characteristics and assumed a uniform consistency of its tissue for the purposes of modeling. Furthermore, it has been established that the oxygen diffusion coefficient fluctuates in multiple ILT layers [32]. Hence, one limitation of the prior computational models is how to estimate differences in oxygen transport regarding different ILT structural features. Improvements to ILT modeling can be made by applying unique properties to each individual layer as suggested by [33].

An insignificant effect of variation in ILT constitutive properties on aortic wall stress has been previously observed by Vorp et al. in [19] using an impermeable model. However, a more recent study [11] suggests that the permeable structure of the ILT may influence its role in AAA rupture. The effects of porous structure modeling have been explored earlier for soft tissues including large arteries [34–38]. ILT tissue contains large water content and is permeable to plasma fluid flow, which can affect oxygen transport within the aneurysmal wall. The range of ILT's permeability measurements reported in the literature is wide [39], which is undoubtedly due to the heterogeneity of the multi-layered material and its age at the time of experimental permeability assessment. Moreover, the ILT porous structure varies spatially as well. However, to our knowledge, the values of these parameters have never been measured for different ILT layers. These observations recommend that nonhomogeneous ILT structural composition needs to be handled more cautiously in future AAA simulations (see [10] for a comprehensive summary on ILT structure and mechanical characterization). While there are several porous structure models of AAA available in the literature [40–42], the effect of coupling between oxygen transport, hemodynamics, and fluid flow through the porous media is a missing component. However, it has been shown that the blood flow affects the luminal oxygen transport and local concentrations within the AAA, particularly in the regions of disturbed flow and reattachment [43]. These previous models include ILT through a porous [40] or poroelastic [44] medium but often in idealized geometries of aneurysms, or by neglecting the contribution of oxygen transport in rupture assessment of AAA [41,45].

It has been suggested that ILT tissue porous properties do not affect wall stresses [45], however, the related effects on oxygen flow needs to be explored as well. Sun et al. [46] performed a parametric study on a patient-specific AAA model, varying the oxygen diffusivity values within an impermeable ILT, and concluded that varying the oxygen diffusivity in the

physiological range did not significantly change the wall oxygen concentration. Loffredo et al. studied the effects of permeability on shear stresses in a descending thoracic aneurysm but did not consider the oxygen transport [47]. Prior investigations show the poroelastic behavior with variation in thrombus permeability but without considering the oxygen diffusivity contribution to the mass transport [44,47]. In summary, the aforementioned studies above have concluded that the integration of porous medium to model thrombus influences local shear stress and oxygen concentrations and the observations are linked to its permeability [47] but have failed to emphasize the combined effects of oxygen diffusivity and permeability and to which extent they play a key role. Our laboratory has previously developed a computational model of oxygen transport in an idealized AAA which contains a one-layer porous ILT [48]. Our earlier studies in [48,49] have thoroughly explored the effect of varying ILT biomechanical parameters such as permeability and oxygen diffusivity in an idealized AAA model. We have also explored the contribution of ILT on oxygen flow in patient-specific AAA geometries using fluid-structure interaction (FSI) methodology [50], as well as the effects of ILT oxygen diffusivity coefficient [49]; however, in a non-porous ILT model. In summary, previous porous ILT models are very limited and all of them assume that ILT has a uniform structure. In addition, most of them have not investigated oxygen transport.

The objective of this study is to consider the multi-layered, heterogeneous structure of the ILT to investigate the relation between its porous structure and oxygen flow to the aneurysmal wall. We augment our previous computational coupled fluid–porous structure—mass transport model for AAA [48] via a parametric study of ILT structural features with the purpose of systematically investigating the influence of changing ILT oxygen diffusivity D_{ilt} and permeability K_{ilt} on oxygen flow in both idealized and patient-specific AAAs. To the best of our knowledge, this is the first study which takes into account the multi-layer structure of the porous ILT and analyzes oxygen transport. Computational results including oxygen contours and filtration velocities inside ILT are presented and discussed.

2. Materials and Methods

Computational models of AAAs containing ILT are constructed in a similar way to the previous research by authors, presented in [49]. The model consists of three domains: the blood in the lumen, the ILT, and the aneurysmal wall. In order to explore how the structure of ILT affects oxygen transport, two layers for the ILT region are considered. In particular, we examine AAA geometries that either lack an ILT, contain a one-layer ILT, or contain a two-layer ILT. A schematic of the three-dimensional CAD models of axisymmetric AAAs is shown in Figure 1a.

The AAA models were designed in the commercially available Fusion 360 CAD software and meshed using the ANSYS SpaceClaim geometry component in ANSYS Workbench (version 22.2, ANSYS Inc., Canonsburg, PA, USA). For each geometry, the AAA domain is set to be 24 cm long [51] with an arterial wall thickness of 0.1 cm. The blood vessel is defined with a radius of R = 1 cm [52] at the inlet and outlet, with a bulge diameter (BD) of 7 cm [27,53]. Both the one-layer and two-layer ILT models are constructed with a length of 8 cm. The luminal ILT and abluminal ILT are modeled as two separate layers, and the total thickness of ILT is 1.5 cm, considered within the range of patient data in [54]. As reasonably assumed by [19], one-third of the total two-layer ILT medium thickness is the luminal layer while two-thirds of the thickness is the medial and abluminal layers. A visual comparison of the geometries is demonstrated in Figure 1.

In the following, we summarize the mathematical model and governing equations. The subscripts f, w, and ilt denote the lumen, the arterial wall, and the ILT domain, respectively, and review the models used in this study. A summary of material properties and all model parameters for AAA domains is provided in Table 1.

Domain	Parameter Description	Parameter Value
Blood (Incompressible Fluid) Arterial Wall (Porous Solid)	Density ρ_f	1050 kg/m^3
	Dynamic viscosity μ_f	0.0035 kg/m.s
	Oxygen diffusivity D_f	$1.6 \times 10^{-9} \mathrm{m}^2/\mathrm{s}$ [55]
	Reynolds number	1100 [56]
	Inlet oxygen concentration C_f^{in}	$5.12 \times 10^{-3} \text{ kg/m}^3 [27]$
	Vasa vasorum oxygen concentration	$2.06 \times 10^{-3} \text{ kg/m}^3 [57]$
	Density ρ_w	1000 kg/m^3
	Oxygen diffusivity D_w	$1.08 \times 10^{-9} \mathrm{m}^2/\mathrm{s}$ [58]
	Permeability K_w	$1.05 \times 10^{-15} \text{ m}^2$
	Porosity γ_w	0.6 [42]
	Reaction rate	$8.4 \times 10^{-3} \text{ s}^{-1}$ [27]
	Interfacial area density IAD	$11,923~{ m m}^{-1}$
	Transfer coefficient $ au$	$3.75 \times 10^{-4} \text{ s}^{-1}$
ILT (Porous Solid)	Density ρ_{ilt}	1000 kg/m^3
	Porosity γ_{ilt}	0.8 [42]
	Interfacial area density IAD	$11,923 \text{ m}^{-1}$
	Transfer coefficient $ au$	$3.75 \times 10^{-4} \text{ s}^{-1}$
	Oxygen diffusivity D_{ilt}	Refer to Table 2
	Permeability K_{ilt}	Refer to Table 2

Table 1. Physical and compositional parameters for AAA domains.

Table 2. Parameter sets for simulated cases. The different values for oxygen diffusivity and permeability are listed for Case 0 to 8. Case 0 represents the case without the ILT, hence there are no values for oxygen diffusivity and permeability. Cases 1, 2, 3, 5, 6, and 7 contain one-layered ILT models, and Cases 4 and 8 contain two-layered ILT models with distinct luminal and abluminal layers.

	D_{ilt} (m ² /s)	K_{ilt} (m ²)
Case 0 (No ILT)	-	-
Case 1	$D_{min} = 1.08 \times 10^{-9}$	$K_{avg} = 1 \times 10^{-11}$
Case 2	$D_{max} = 1.60 \times 10^{-9}$	$K_{avg} = 1 \times 10^{-11}$
Case 3	$D_{avg} = 1.34 \times 10^{-9}$	$K_{avg} = 1 \times 10^{-11}$
Case 4 (bilayered)	Ü	Ü
Abluminal	$D_{min} = 1.08 \times 10^{-9}$	$K_{avg} = 1 \times 10^{-11}$
Luminal	$D_{max} = 1.60 \times 10^{-9}$	$K_{avg} = 1 \times 10^{-11}$
Case 5	$D_{avg} = 1.34 \times 10^{-9}$	$K_{min} = 1 \times 10^{-15}$
Case 6	$D_{avg} = 1.34 \times 10^{-9}$	$K_{max} = 1 \times 10^{-7}$
Case 7	$D_{avg} = 1.34 \times 10^{-9}$	K gradual change
Case 8 (bilayered)		
Abluminal	$D_{avg} = 1.34 \times 10^{-9}$	$K_{min} = 1 \times 10^{-15}$
Luminal	$D_{avg} = 1.34 \times 10^{-9}$	$K_{max} = 1 \times 10^{-7}$

2.1. Blood Flow in the Lumen

Blood flow in the lumen is assumed to behave as an incompressible, Newtonian viscous fluid since the aorta is a large artery. Blood flow is also considered to be laminar and steady. Therefore, flow inside the artery is described by the Navier–Stokes equations:

$$\rho_f \Big(\mathbf{U}_f. \, \nabla \mathbf{U}_f \Big) = \nabla.\sigma_f \qquad in \, \Omega_f \tag{1}$$

$$\nabla . \boldsymbol{U}_f = 0 \qquad in \ \Omega_f \tag{2}$$

Here, ρ_f stands for blood density. $\textbf{\textit{U}}_f$ denotes the blood flow velocity field with $\sigma_f = -p_f \textbf{\textit{I}} + 2\mu_f \textbf{\textit{D}}(\textbf{\textit{U}}_f)$ as the fluid Cauchy stress tensor, where p_f and μ_f define the blood pressure and dynamic viscosity, respectively. The symmetric part of the blood velocity gradient is given as $\textbf{\textit{D}}(\textbf{\textit{U}}_f) = \frac{1}{2} \Big(\nabla \textbf{\textit{U}}_f + \nabla \textbf{\textit{U}}_f^T \Big)$.

The oxygen transport in the lumen is modelled by the convection-diffusion equation:

$$\nabla \cdot \left(-D_f \nabla C_f + \mathbf{U}_f C_f \right) = 0 \qquad in \ \Omega_f \tag{3}$$

 C_f and D_f denote the oxygen concentration in the lumen and oxygen diffusion coefficient in the blood, respectively. The effect of oxygen binding to hemoglobin on oxygen concentrations in the lumen is neglected, considering that the focus here is on comparisons of relative transport over the arterial wall and ILT.

2.2. Aortic Wall and Intraluminal Thrombus

In order to capture the influence of the interstitial flow on oxygen transport, the ILT and arterial wall tissues are modeled as porous regions using the Brinkman equation. The porous model, following the theory of mixtures, assumes that fluid and solid phases co-exist and both phases are permeable to oxygen. The mass and momentum balance equations are given as:

$$\nabla \cdot \left(\rho_f (\mathbf{U}_p \times \mathbf{U}_p) \right) - \nabla \cdot \left(\mu_f \left(\nabla \mathbf{U}_p + \left(\nabla \mathbf{U}_p \right)^T \right) \right) = -\frac{\mu_f}{K} \mathbf{U}_p - \nabla p_p \quad in \ \Omega_w \cup \Omega_{ilt}$$

$$\nabla \cdot \mathbf{U}_p = 0 \quad in \ \Omega_w \cup \Omega_{ilt}$$
(4)

where U_p and p_p refer to the fluid velocity and pressure inside the porous media, respectively. The variable U_p is also known as intramural flow or filtration velocity. The parameter K is the permeability coefficient, which is permitted to differ between the wall and ILT; particularly, K_{ilt} and K_w define the ILT and wall permeability values.

The advection-diffusion-reaction equation, which accounts for convective oxygen transport as well as the consumption of oxygen in smooth muscle cells, is used to model the oxygen transport in the arterial wall tissue:

$$\nabla \cdot (-D_w \nabla C_w + \mathbf{U}_v C_w) = S \qquad in \Omega_w \tag{5}$$

Here, C_w is the oxygen concentration in the arterial wall that has a correlation with wall porosity (γ_w) and oxygen concentrations in the fluid $(C_{w,f})$ and the solid $(C_{w,s})$ phases of the porous wall domain as $C_w = \gamma_w C_{w,f} + (1 - \gamma_w) C_{w,s}$. The parameter D_w defines the wall oxygen diffusivity. Furthermore, S is the reaction term that accounts for the metabolic consumption of oxygen and is assumed to be linearly proportional to cell availability, $S = (1 - \gamma_w) \ r C_w$, and the constant r is defined as the oxygen reaction rate [59], obtained under the assumption that the volume flux of oxygen is completely consumed by the smooth muscle cells.

Similarly, oxygen transport in the porous ILT is modeled by the advection-diffusion equation, given by:

$$\nabla \cdot (-D_{ilt} \nabla C_{ilt} + \mathbf{U}_{p} C_{ilt}) = 0 \qquad in \ \Omega_{ilt}$$
 (6)

Here, C_{ilt} denotes the oxygen concentration in the ILT that has a correlation with ILT porosity (γ_{ilt}) and oxygen concentrations in the fluid $(C_{ilt,f})$ and the solid $(C_{ilt,s})$ phases of the porous ILT domain as $C_{ilt} = \gamma_{ilt}C_{ilt,f} + (1 - \gamma_{ilt})C_{ilt,s}$. The parameter D_{ilt} defines the ILT oxygen diffusivity. ILT has no smooth muscle cells; therefore, it is assumed that there is no oxygen consumption in the ILT.

Finally, the transfer coefficient (τ), and interfacial area density (IAD) for both the wall and ILT regions are computed. The detail of the calculation procedure is provided in [48,59], and the resulting values are listed in Table 1. These coefficients account for the transfer of oxygen molecules between the fluid and solid phases within the porous media in both ILT and wall tissues.

2.3. Parameter Identification

To evaluate the effects of physiologic variations of oxygen diffusion coefficient D_{ilt} and permeability K_{ilt} , as well as the bilayered structure of ILT on the oxygen distribution within AAA tissue, a parametric study is conducted as follows. Nine finite element models were constructed from Cases 0 to 8, all with the same geometries described earlier. Each model is distinct by the variation of the ILT structural parameters D_{ilt} and K_{ilt} . Because the patient-specific ILT porous properties and the oxygen diffusivity of the inner and outer ILT layers are not known, multiple modeling paradigms are considered (Table 2). Case 0 represents the AAA with no ILT model and is developed for comparison purposes. Cases 1, 2, 3, 5, 6, and 7 consist of a one-layered ILT assuming homogeneity of the ILT region. Additionally, to evaluate the effects of a non-homogeneous ILT structure, a bilayered model is created by dividing the ILT thickness into two layers, representing the luminal and abluminal regions. Cases 4 and 8 are simulated using this two-layered ILT model.

The range of the values describing the ILT oxygen diffusivity is determined from previous studies by Moore and Ethier [58] and Sun et al. [46]. Specifically, we considered a range of oxygen diffusivity values for the thrombus region where D_{min} is based on the diffusivity of oxygen through the wall, $D_w = 1.08 \times 10^{-9}$ m²/s obtained from [60,61] and the value for D_{max} is based on the diffusivity of oxygen in the blood plasma, $D_f = 1.6 \times 10^{-9}$ m²/s which is consistent with the prior investigations in [55,62]. A mean value of $D_{avg} = (D_f - D_w)/2$ is also chosen for the average oxygen diffusivity in the ILT which equates to 1.34×10^{-9} m²/s. ILT permeability parameter K_{ilt} is found to be from 10^{-18} m² [63] to 10^{-7} m² [40]. Therefore, the range of permeability values is adopted from studies by [40,47] where we define 10^{-15} m² as the minimum (K_{min}), 10^{-7} m² as the maximum (K_{max}), and 10^{-11} m² as the average (K_{avg}) values. The permeability of the wall is assumed as $K_w = 1.05 \times 10^{-15}$ m² for all the simulations.

Simulations are performed to compare oxygen distribution patterns in Cases 1-4, where K_{ilt} is kept constant with its average value of 10^{-11} m² and D_{ilt} is varied. Specifically, in Case 1 we use the constant minimum oxygen diffusivity equal to 1.08×10^{-9} m²/s, while in Case 2 we use maximum oxygen diffusivity of 1.60×10^{-9} m²/s. In Case 3 we use an average of both oxygen diffusivity and permeability values in the ILT region. Case 4 is a two-layered model with oxygen diffusivity values of 1.08×10^{-9} m²/s and 1.34×10^{-9} m²/s for luminal and abluminal layers, respectively. Cases 5, 6, 7, and 8 are simulated with the average value of D_{ilt} , but we varied the permeability. In Case 5 we use a constant permeability equal to the minimum permeability 10^{-15} m², in Case 6 we use the maximum permeability 10^{-7} m² and in Case 7 we use a gradual change in permeability. In Case 7 a gradient of permeability is proposed to represent the layered structure of ILT by considering a gradual change in permeability through the ILT thickness due to the heterogeneity of the material. The gradient of permeability is obtained by solving a 3D Poisson equation defined on the ILT region with Dirichlet boundary conditions and capturing a distribution of this model parameter. The boundary conditions are defined to be equal to K_{max} on the luminal surface and K_{min} on the abluminal surface of ILT that is in contact with the arterial wall. It should be noted that the permeability parameter decreases through the ILT thickness according to [11,64], since luminal ILT has a looser network than the abluminal ILT [15] and therefore larger permeability and diffusivity coefficients. Case 8, which is a two-layered model, has the minimum and maximum permeability of 10^{-15} and 10^{-7} m² in abluminal and luminal layers, respectively.

2.4. Computational Details and Boundary Conditions

In this section, the computational approach and boundary conditions are summarized. A fully developed unidirectional velocity profile $\boldsymbol{U}_f^{in}=0.3~\text{m/s}$ is applied at the inlet of the lumen. The flow rate is chosen to match physiological Reynolds numbers in the abdominal aorta under the resting condition [65]. In particular, the Reynolds number of 1100 based on the entrance lumen diameter and the inlet flow condition is obtained, which is within the realistic range for Reynolds numbers in the abdominal aorta [56].

The inlet oxygen concentration is $C_f^{in} = 5.12 \times 10^{-3} \, \text{kg/m}^3$, calculated by assuming a uniform inlet oxygen partial pressure of 100 mmHg [66] and by using the molar mass of oxygen. At the outlet, the reference pressure value is applied, which can be arbitrarily set for incompressible flow. The arterial wall exterior surface is modeled as an opening boundary condition which allows the fluid to cross the boundary surface in either direction; enabling oxygen to either exit through the wall or enter the tissue. The influence of the vasa vasorum on this boundary is modeled by imposing the partial pressure of oxygen. Specifically, the abluminal wall partial pressure is fixed at 50 mmHg [57], as experimental studies showed that the level of adventitial oxygen tension is half of the oxygen tension in the blood [60,67]. A zero-flux condition is prescribed on the normal direction n of the two end cross-sectional areas of the arterial wall. The walls are rigid with a no-slip condition.

The model is complemented by the following continuity conditions and the conservative interface flux condition for oxygen at the interface between the ILT and the wall, and the ILT and the lumen:

$$C_{f} = C_{w}, \qquad \left(\mathbf{U}_{f} C_{f} - D_{f} \nabla C_{f}\right) \cdot \mathbf{n} = \left(\mathbf{U}_{p} C_{w} - D_{w} \cdot \nabla C_{w}\right) \cdot \mathbf{n} \qquad on \ \Gamma_{f-w}$$

$$C_{f} = C_{ilt}, \qquad \left(\mathbf{U}_{f} C_{f} - D_{f} \nabla C_{f}\right) \cdot \mathbf{n} = \left(\mathbf{U}_{p} C_{ilt} - D_{ilt} \cdot \nabla C_{ilt}\right) \cdot \mathbf{n} \qquad on \ \Gamma_{f-ilt} \qquad (7)$$

$$C_{ilt} = C_{w}, \qquad \left(\mathbf{U}_{p} C_{ilt} - D_{ilt} \cdot \nabla C_{ilt}\right) \cdot \mathbf{n} = \left(\mathbf{U}_{p} C_{w} - D_{w} \cdot \nabla C_{w}\right) \cdot \mathbf{n} \qquad on \ \Gamma_{ilt-w}$$

Moreover, on the interface between the lumen and wall, and the lumen and ILT a conservative interface flux condition for the filtration flow is applied. For a multilayer ILT model there is also an additional condition between ILT layers, where $\Gamma_{ilt\ 1-2}$ indicates the interface between luminal (index 1) and abluminal (index 2) layers:

$$C_{ilt-1} = C_{ilt-2},$$

$$(\boldsymbol{U}_{p}C_{ilt-1} - D_{ilt-1} \cdot \nabla C_{ilt-1}).\boldsymbol{n} = (\boldsymbol{U}_{p}C_{ilt-2} - D_{ilt-2} \cdot \nabla C_{ilt-2}).\boldsymbol{n} \quad on \ \Gamma_{ilt \ 1-2}$$
(8)

Numerical simulations are performed to simulate blood flow coupled with the oxygen transport in the bloodstream, as well as convective and diffusive oxygen transport in the wall and ILT regions. Fully coupled fluid dynamics and oxygen transport system of Equations (1)–(8) are implemented and numerically solved in ANSYS CFX Workbench software (v.22.2, ANSYS Inc., Canonsburg, PA, USA), by using a monolithic approach. The advection equations are discretized by a flux-corrected upwind scheme, with a conservative length scale and auto timescale. The diffusive terms in the transport equations are discretized by the second-order central differencing scheme, and the convective term in the Navier–Stokes equation is linearized by Picard iterations. The numerical simulations are solved using the domain-decomposition MPI directives in a parallel mode. For the residuals of the linear system of equations, the convergence criteria of 10^{-6} is considered.

The geometries are split into linear tetrahedral elements and a mesh convergence study is performed to assure an optimally sized mesh. Three different mesh densities with sizes from 10^6 to 3×10^6 tetrahedral elements (coarse, medium, and fine mesh) were used for the sensitivity test. The mesh sensitivity test is carried out by monitoring fluid flow solutions as well as the oxygen concentration at some examined sections. The solution was considered mesh-independent for an error lower than 5% in terms of blood velocity and pressure. It has been observed that the maximum difference in wall oxygen concentration between fine and medium mesh was less than 4.2%, but between the medium and coarse mesh was less than 18.7%. Hence, the medium computational mesh consisting of approximately 1.8 million tetrahedral elements is found to be sufficient to obtain grid-independent results.

3. Results

In this section, the computational results, specifically the oxygen concentration measures inside the AAA tissue are obtained and analyzed to investigate the effects of ILT structural composition. Zakerzadeh et al. [48] provided additional results on velocity fields inside the lumen and distribution of the filtration velocities within the arterial wall. Profiles

of oxygen concentration in AAA including the lumen, ILT, and wall domains can also be found in our prior research [48,49].

The contours of oxygen concentration distributions are demonstrated in Figure 2 for each AAA case with ILT included in the analysis. Only the ILT region is plotted, and the contours are obtained on the ILT cross-section that cuts the domain in half.

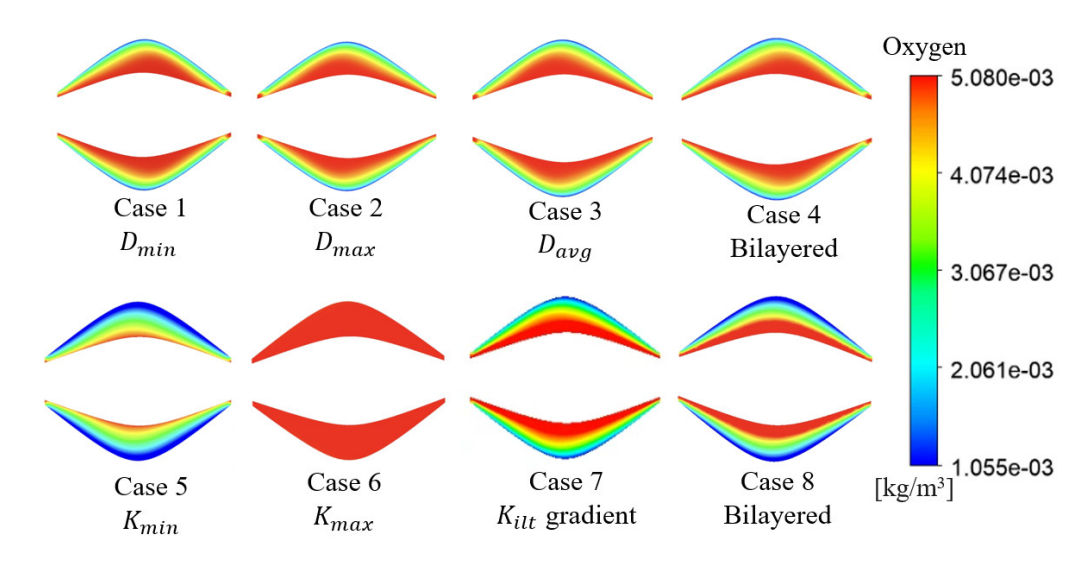


Figure 2. Contours of oxygen concentration in ILT for all analyzed cases (Table 2) on the same scale. Only the ILT region is plotted for each case. Top panel simulations represent cases where the diffusion coefficient is varied in one- and multilayer ILTs. Bottom panel simulations represent cases where permeability is varied in one- and multilayer ILTs.

The contours on the top panel of Figure 2 demonstrate the comparison of the oxygen distributions in the ILT obtained by varying the diffusion coefficient D_{ilt} based on Table 2 protocol, while the bottom panel simulations represent cases where permeability K_{ilt} is varied in one- and multi-layer ILTs. In the top panel of Figure 2, Case 1 has minimum oxygen diffusivity of $D_{min} = 1.08 \times 10^{-9} \text{ m}^2/\text{s}$, Case 2 has maximum oxygen diffusivity of $D_{max} = 1.6 \times 10^{-9}$ m²/s, Case 3 has the average oxygen diffusivity, and finally, Case 4 is a two-layered model and has different D_{ilt} in the luminal and abluminal layer with the values of 1.08×10^{-9} m²/s and 1.6×10^{-9} m²/s respectively. For all the cases, it has been noted that the distribution of oxygen concentration differs across the ILT as shown in the contours indicated by the red color near the lumen, having higher values of oxygen concentration, and blue color at the edge of the tissue that represents the minimum oxygen concentration along the inner wall surface. In the bottom panel of Figure 2, Case 5 has a minimum permeability of 10^{-15} m², and a gradual decrease in oxygen concentration is observed as well. On the contrary, in Case 6 which has maximum permeability of 10^{-7} m², the entire ILT region appears red, representing that the oxygen concentration is the highest when compared to all other cases. Case 8, a two-layer model where the abluminal and luminal layers have permeability values of 10⁻¹⁵ and 10⁻⁷ m², respectively; depicts a similar result with a gradual decrease in oxygen concentration. The abluminal layer has less oxygen concentration, and the luminal layer has more oxygen, which is close to the concentration inside the lumen and is shown by the orange-red color.

It is observed that there are no significant differences in the oxygen distribution profile between Cases 1, 2, 3, and 4, which have different D_{ilt} values but the same permeability. In Cases 5, 6, 7, and 8, with varying permeability K_{ilt} , a distinct change in contours of oxygen concentration in ILT is shown (Figure 2). The highest oxygen concentration within the ILT tissue is observed in Case 6 with $K_{ilt} = 10^{-7}$ m², while the smallest oxygen levels are obtained in Case 5 with $K_{ilt} = 10^{-15}$ m². In comparison, the results obtained with a gradient of permeability show a similar trend to the multilayered ILT model with individual permeability values of K_{min} and K_{max} for luminal and abluminal layers.

Concentrations for all the simulated cases at two locations within the tissue and along the boundaries are presented and compared (Figure 3). In the left panel of Figure 3, the values of the concentration for cases with different D_{ilt} are shown with different line patterns in black, while cases with different K_{ilt} are shown with different line patterns in blue. The concentration for the left plot is taken along a vertical line that starts at the center of the domain. The path line is identified by the yellow color at the top of the plot. The concentration in the luminal domain is relatively constant for all eight cases, and it starts to decrease exponentially at different rates once we reach the ILT interface. However, a significant change in oxygen concentration is observed only for cases with varying K_{ilt} , with the remarkable difference between Cases 5 and 6 which have ILTs with the permeability of K_{min} and K_{max} respectively. In cases with varying D_{ilt} , no significant differences in oxygen concentration within the ILT are noted.

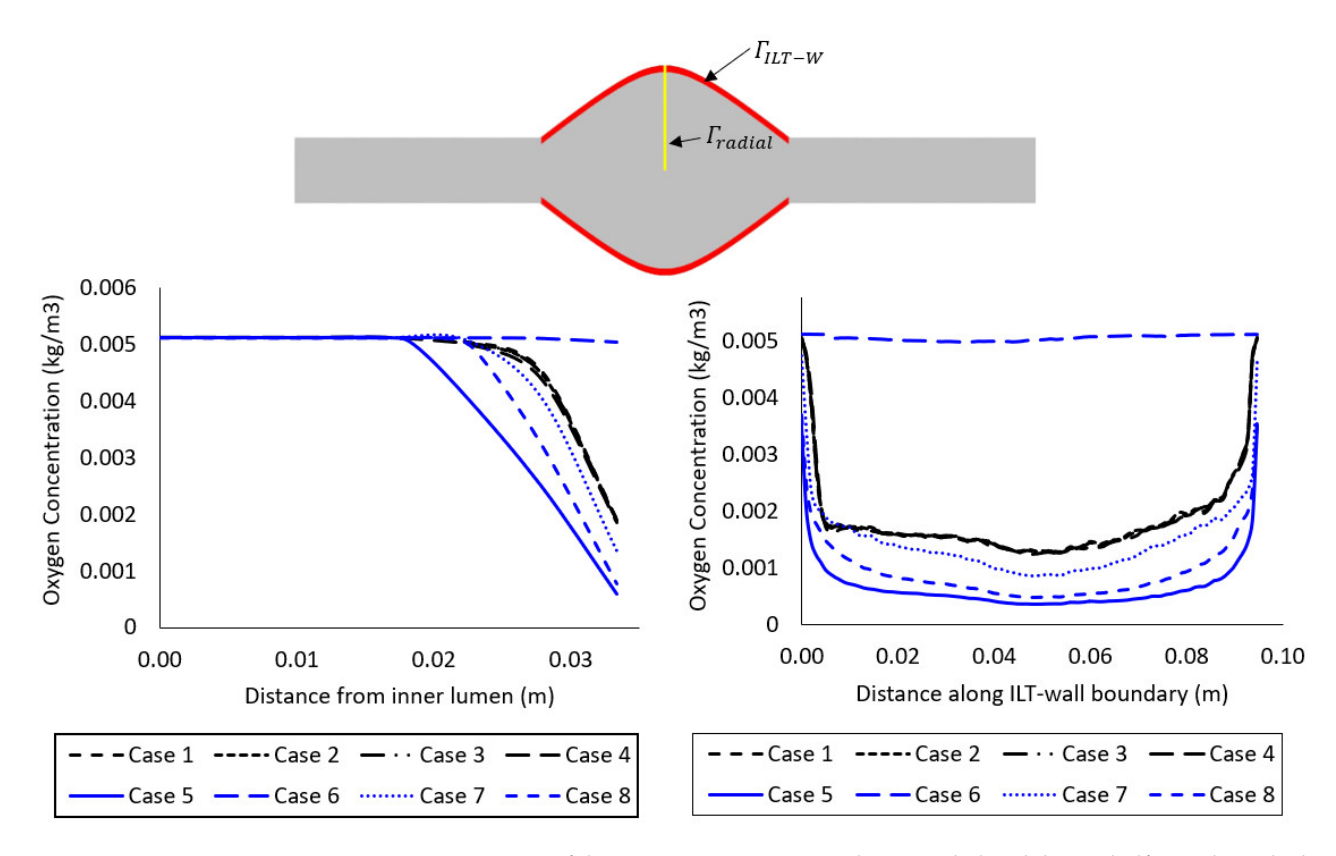


Figure 3. Comparison of the oxygen concentration along a radial path line at halfway along the length of the lumen in the cases with varying ILT oxygen diffusivity (D_{ilt}) (Case 1–4) and ILT permeability (K_{ilt}) (Case 5–8) on the left, and comparison of the oxygen concentration along the axial length on the interior interface of the arterial wall in the same cases (right). Case information for both plots is provided in Table 2. At the top, the path lines are shown with a yellow line, Γ_{radial} for the left plot, and a red line Γ_{ILT-W} for the right plot. The Γ_{ILT-W} represents the interface between the ILT and wall domain. The same eight cases are shown in Figure 2.

Moreover, the oxygen concentration at the inner wall surface (Γ_{w-ilt}) for eight different cases is shown in the right panel of Figure 3. Wall oxygen concentration is captured in the middle portion of AAA where the ILT is located. As before, we notice that the oxygen diffusivity of the ILT does not affect the concentrations on the wall interface, while the ILT permeability does. The greater the permeability of the ILT, the higher the concentration of oxygen on the interface between the ILT and the wall is observed. Simulations also demonstrate that an ILT with smaller permeability results in a much smaller oxygen supply within the wall.

The contours for filtration velocities within the ILT region for cases with varying permeability K_{ilt} are compared in Figure 4 on the logarithmic scale. Cases 3, 5, and 6 have permeability values of K_{avg} , K_{min} , and K_{max} , respectively. In all the cases, we use the baseline values for the rest of the parameters, as summarized in Tables 1 and 2. Plots are obtained on the cross sections at the same planes used in Figure 2. By altering ILT permeability, high variations of filtration velocity are observed, hence a logarithmic scale is used.

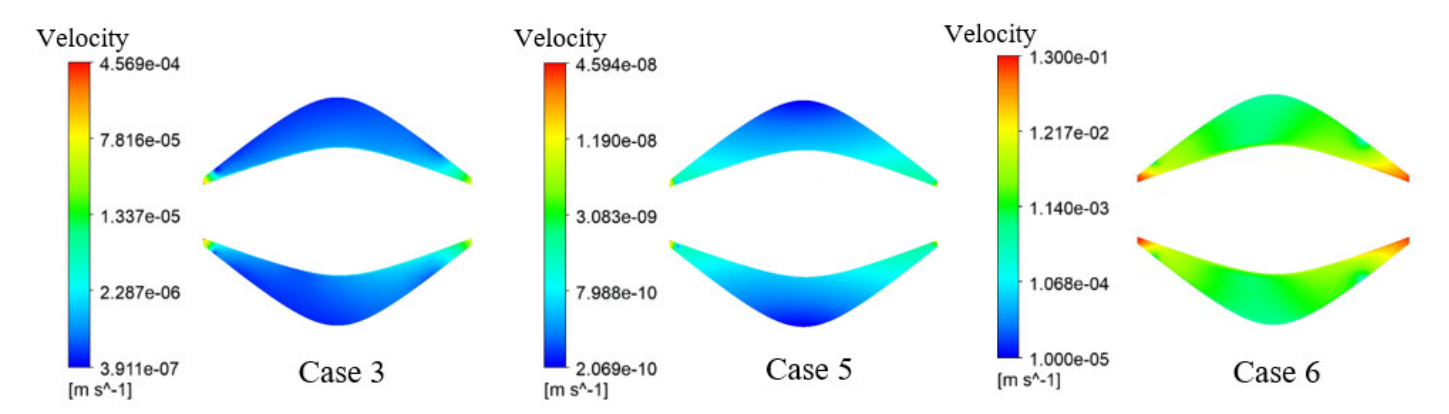


Figure 4. Contours showing the distribution of ILT filtration velocities (i.e., flow through the porous ILT tissue) for cases with varying ILT permeability on the logarithmic scale (Case 3 with K_{avg} , Case 5 with K_{min} , and Case 6 with K_{max}). Contour colors show the magnitude of the interstitial flow. In the insets, the velocity contour is shown for the ILTs only, and each case with its own scale.

It is found that there is a meaningful dependence of the interstitial flow velocity on the permeability values. More precisely, by decreasing ILT permeability from Case 6 to Case 3 and then to Case 5 in Figure 4, the filtration velocity has the average range of 10^{-3} m/s, 10^{-7} m/s, and 10^{-10} m/s respectively. This indicates that when ILT tissue permeability is decreased, the interstitial flow in the ILT decreases, as expected. The ILT region with maximum permeability has the maximum filtration velocity as it is easiest for the intramural fluid to flow through; while the region with minimum permeability has the minimum velocity as it is difficult for the fluid to pass across the ILT region in AAA. The greatest distinction is shown for increasing the K_{ilt} from its average value, and there are 4 orders of magnitude difference between those recorded for the highest permeability versus the lowest one.

For all simulated cases (Table 2), a measurement of average oxygen concentration over the arterial wall region is also defined, denoted by $\overline{C_w}$, and its percentage of the difference between the cases with an ILT and the case without an ILT is obtained using Equation (9). The results are compiled in Table 3 and shown in Figure 5.

$$\overline{C_w} = \frac{\int_{\Omega_w} C_w \, d\Omega_w}{\int_{\Omega_w} d\Omega_w}
\delta_{\overline{C_w}} = \left| \frac{\overline{C_w}_{w/o \, ILT} - \overline{C_{ww/ILT}}}{\overline{C_{ww/o \, ILT}}} \right| \times 100\%$$
(9)

Table 3. Volumetric average of oxygen concentration in the arterial wall $\overline{C_w}$ and percent difference of
oxygen concentration in wall in reference to Case 0, computed using Equation (9).

Case ID	$\overline{C_w}$ (kg/m 3) $ imes$ 10 $^{-3}$	$\delta_{\overline{C_w}}$ (%)
0	1.793	0
1	1.221	31.89
2	1.224	31.74
3	1.223	31.81
4	1.217	32.14
5	0.946	47.47
6	1.790	0.18
7	1.116	37.75
8	0.974	45.70

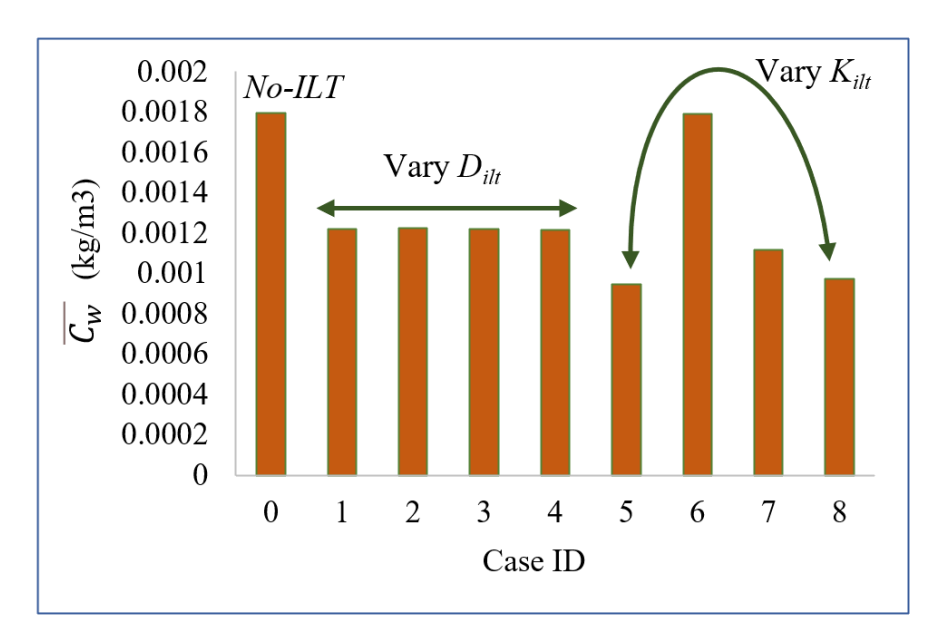


Figure 5. Volumetric average of oxygen concentration in the arterial wall for the nine simulated cases based on the information provided in Table 3. Case 0 is without ILT.

Table 3 and Figure 5 indicate that the total oxygen transported to the arterial wall decreases with the presence of the ILT, whether the thrombus contains one or two layers. The case without the ILT (Case 0) has an average oxygen concentration in the AAA wall of 1.793×10^{-3} kg/m³, and each case, all of which contain an ILT, has an average oxygen concentration value less than that of Case 0. Specifically, one-layer Cases 1, 2, and 3 are calculated to have an average oxygen concentration of $1.221 \times 10^{-3} \text{ kg/m}^3$, $1.223 \times 10^{-3} \text{ kg/m}^3$, and 1.222×10^{-3} kg/m³, respectively. The average wall oxygen concentration for Case 1, which has the minimum oxygen diffusivity, decreases by 31.89%, and in Case 2, which has the maximum oxygen diffusivity, decreases by 31.74%. Case 3 has the average oxygen diffusivity and permeability values, and a decrease of wall oxygen by 31.81% with respect to Case 0. Case 4 has a similar percent decrease of 31.14% and an average oxygen concentration of $1.217 \times 10^{-3} \text{ kg/m}^3$. This case contains two layers, the luminal layer has the maximum oxygen diffusivity value and the abluminal layer has the minimum. Case 5 with the smallest permeability value has the largest percent decrease of 47.47% with an average volumetric oxygen concentration of 9.455×10^{-4} kg/m³. Case 6, which has the highest permeability, has the smallest percent decrease of 0.18%. The average oxygen concentration of $1.789 \times 10^{-3} \text{ kg/m}^3$ is slightly less than that of Case 0. Case 7, which is characterized by a gradual change in K_{ilt} , shows a percent decrease of 37.75% and has an average oxygen concentration of 1.116×10^{-3} kg/m³. When Case 7 is compared with other

cases, it is noticed that the 37.75% decrease is more than the cases with varying D_{ilt} . The second two-layer case, Case 8, has the maximum permeability in the luminal layer and the minimum permeability in the abluminal. This case has an average oxygen concentration of $9.738 \times 10^{-3} \text{ kg/m}^3$ and a percent decrease of 45.70% with respect to Case 0.

In summary, it has been observed that Case 5, which has the smallest permeability, has less oxygen in the wall due to less oxygen filtration compared to Case 3 with the average permeability. Case 6 with maximum permeability has more oxygen in the wall due to higher oxygen transport via filtration and convection (Figure 5). Case 8 with a multi-layer ILT has less oxygen than Case 3 with average ILT permeability since overall permeability is lower. In this case, the abluminal layer with small permeability is thicker than the luminal layer; however, it has more oxygen than Case 5 with K_{min} permeability. Figure 5 also shows that varying oxygen diffusivity of ILT does not affect the wall oxygen supply. Case 0 with no ILT appears to have the highest wall oxygen concentration.

Finally, a patient-specific case is considered to demonstrate the applicability of the framework to anatomically realistic AAA geometries. A model built from CT-angioscans of a patient with AAA is adopted. The detailed elaboration of this framework is provided in [50]. A uniform systolic pressure of $p_f^{in}=130$ mmHg at the inlet [68] and a mass flow rate of 0.075 kg/s [69] at the outlet of the fluid domain are applied as boundary conditions; the resulting Reynolds number of 1600 is within the realistic range in the abdominal aorta at rest [56]. The mesh resolutions of the patient-specific case are identical to those reported in the computations of [50]. The cited study documents a systematic convergence testing and shows the effects of spatial refinement on quantities of interest relating to AAA biomechanics. The results of this testing indicate that those quantities of interest are resolved to within a few percent at the resolution used.

To focus on the thrombus, the 3D geometry of the aneurysmal zone is modeled (Figure 6a). Figure 6b demonstrates blood velocity streamlines and the recirculation zone at the bulge, where velocity is the slowest. To avoid excessive computational time, a parametric study on only ILT permeability is performed and a constant value of oxygen diffusivity $D_{avg} = 1.34 \times 10^{-9} \text{ m}^2/\text{s}$ is considered. Specifically, ILT permeability values of $K_{ilt} = 10^{-7}$, 10^{-11} , and 10^{-15} m² are simulated.

Oxygen concentration contours over a cross-sectional region in the ILT of the patient-specific geometry for each case are demonstrated in Figure 6c. The cross-section surface is located at the AAA bulge (Figure 6c), and is kept consistent between the cases. The pattern of oxygen distribution in these three contours indicates that oxygen concentration values are the greatest at the interface between lumen and ILT and diffuse across the ILT thickness. More precisely, the cases with the minimum and average permeability values, 10^{-15} and 10^{-11} m², respectively, demonstrate a gradual decrease in oxygen concentration inside the tissue where the minimum value is reached on the wall of the abluminal surface (Figure 6). This is indicated by the blue color at the edge of these cross-sections.

Cross-sectional contours show an increase in oxygen concentration with increasing permeability (left to right). In comparison to the case with the smallest permeability, the cross-section of the ILT with the average permeability shows a higher concentration of oxygen in the region in contact with the lumen, which is represented by the red-colored interior of the cross-section. The cross-section at the far right of Figure 6c depicts the oxygen concentration contour of the case with the highest permeability, 10^{-7} m². This case, similar to the idealized model with the same permeability, yielded a significantly higher oxygen concentration along the interface between the ILT and the arterial wall. Specifically, the entire ILT region is red, indicating that the oxygen concentration along this section increases compared to the smaller permeability values. In particular, the change in permeability causes noticeable differences in concentration patterns between $K_{max} = 10^{-7}$ and $K_{avg} = 10^{-11}$ m², while between $K_{avg} = 10^{-11}$ and $K_{min} = 10^{-15}$ m² changes are minimal.

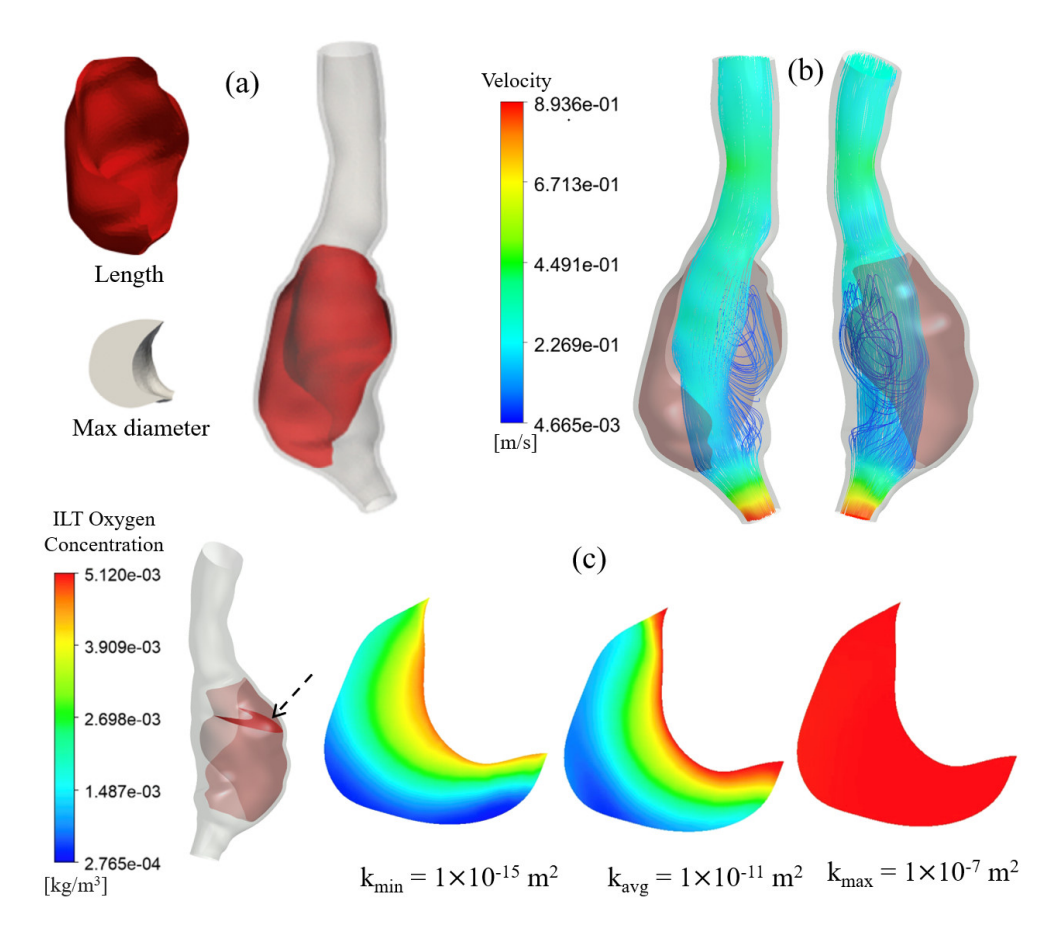


Figure 6. Illustration of (a) The patient-specific AAA geometry used in numerical simulations. The lumen and arterial wall are shown in grey, while the ILT is shown in red. See [50] for geometric features of AAA and contained ILT; (b) Velocity streamlines through the lumen of the AAA geometry; (c) Oxygen concentration contours on a selected ILT cross-section (shown in red and indicated by arrow) for cases with different permeability K_{ilt} values.

4. Discussion

This research aims to develop a computational framework of an AAA including a multi-layered porous medium mimicking the ILT presence to investigate the influence of its layered structure as well as the significance of integrating a permeable thrombus on oxygen transport. Prior computational models of AAAs considered the coupling between hemodynamics and mass transport by modeling the ILT tissue as an impermeable material (i.e., [40,46]). We have previously developed a coupled blood flow-oxygen transport model incorporating advection, diffusion, and reaction [48]; to offer a step forward in addressing the transport of biomolecules in AAA and their interaction with the arterial wall living tissue. However, ILT was assumed to be a uniform tissue with an idealized geometry in the aforementioned study. Incorporating the patient-specific and multilayer structure of the ILT into our framework and analyzing quantitatively the influence of ILT compositional features on the oxygen metrics and concentration attenuation in the arterial wall is the contribution of this paper.

As expected, a gradual change in oxygen concentrations inside the ILT tissue in all cases is observed, with the maximum concentration on the ILT luminal surface and the minimum value on the ILT abluminal surface (Figure 2). Comparing oxygen contours of Figure 2 in cases with varying oxygen diffusivity in ILT suggests that concentrations in the wall do not change significantly, indicating that the results are not very sensitive to the value for diffusion coefficient as long as it is within the chosen range. However, comparisons among cases with varying permeability reveal that the oxygen concentrations are sensitive to the filtration flow.

Regardless of the ILT stratification, oxygen concentration on the interface between the ILT and the arterial wall is consistently higher in the case with higher ILT permeability (right panel of Figure 3), while lower permeabilities decreased the concentration. The results indicate that D_{ilt} does not affect the filtration velocity, and therefore oxygen concentration pattern in the wall in a sensitive manner. Simulations can also help to evaluate the role of extracellular fluid flow and impact of reducing intrinsic permeability on mass transport within the arterial wall. It has been demonstrated that a smaller ILT permeability results in lower interstitial flow velocity and therefore lower oxygen levels on the inner wall surface (Figure 4), while a higher oxygen level is observed in higher ILT permeability values.

Results in Figure 5 and Table 3 suggest that the variation of ILT properties within the physiological range for diffusivity and permeability parameters results in a maximum of 47% difference in the wall oxygen supply prediction. This value is computed considering that the maximum difference between Case 0 and all the other cases is 47%, related to Case 5 with minimum permeability, while the minimum difference between Case 0 and other simulated cases is less than 1%, which corresponds to Case 6 with maximum permeability. If this 47% variation is acceptable, then there is no need for determining patient-specific permeability parameters for ILT and the mean permeabilities can be used for a one-layer case. It should also be noted that variations of oxygen diffusion coefficient within ILT resulted in less than a 1% difference in wall oxygen supply (Table 3) between Case 1 and Case 2 with minimum and maximum oxygen diffusivity values.

The predicted blood velocity magnitude for both idealized and patient-specific models is within the range of experimental measurements of AAA hemodynamics (25-60 cm/s in the normal section of the aorta [65]), and the resulting Reynolds numbers of 1100 and 1600 for the idealized and patient-specific cases, respectively, are within the realistic range in the abdominal aorta at rest [56]. Moreover, results for the oxygen levels within the aneurysmal tissue and filtration velocity magnitude show good correspondence with prior investigations. Due to the low wall permeability, the magnitude of the interstitial velocity is very small, however, the model yielded the filtration velocity in the expected order of magnitude from the literature (1.76 \times 10⁻⁸ m/s in [70] and the range of 10⁻⁸–10⁻⁷ m/s in [42], both within limits of K_{avg} values). The oxygen transport model is validated in Zakerzadeh et al. [49] using idealized AAA geometries, and the obtained oxygen concentration profiles reported in the cited study were consistent with Vorp et al. [27]. The oxygen profiles on the ILT-wall interface were also tested against experimental data for a large group of patients with thin and thick ILT in [26] and the qualitative agreement was observed. However, it is difficult to find suitable clinical or in vitro data for quantitative validation since precise details, such as the variation in wall thickness, ILT thickness, and the presence of vasa vasorum can significantly affect the outcome.

In summary, the observations suggest that explicit incorporation of ILT multilayer structure in the computational analysis is unlikely to substantially alter oxygen measures in comparison to models assuming a homogenous thrombus, provided that the ILT permeability coefficient is the same between models. Our results also show that under a nonhomogeneous layered ILT assumption, the choice of ILT permeability from values common in the literature can result in significantly larger variations in oxygen predictions compared to the effects of oxygen diffusivity. Changing the values of D_{ilt} within the chosen range had only a moderate effect on the oxygen distribution while adopting the nonhomogeneous ILT featuring two sets of permeability parameters, one for the inner layer and one for the outer layer, alters the oxygen distribution significantly.

For the patient-specific simulation, it has been found that changes in the permeability values demonstrate a significant effect on the oxygen flow within the tissue. A smaller ILT permeability causes less oxygen to reach the arterial wall, which is linked to hypoxia, and a larger ILT permeability results in a greater oxygen concentration along the interior of the aortic wall. When K_{ilt} is increased, the filtration flow and therefore the oxygen concentration in the ILT increased, as expected. Oxygen concentration decreased slightly across the ILT with a decrease in permeability from its average value. By increasing

the K_{ilt} further to 10^{-7} m², the oxygen concentration increases significantly (Figure 6). However, the concentration results are not highly sensitive to the ILT permeability of less than 10^{-11} m². This threshold value is in agreement with the observations in [42] which indicates that the permeability of that range does not causes a change in filtration velocity.

In this work, the inlet velocity boundary conditions are assumed constant. Towards the scope of this work, in analyzing the impact of wall permeability on oxygen concentration, this assumption is not expected to produce an alternative conclusion on varying D_{ilt} and K_{ilt} , though the implications should be addressed. For this study, we first note the velocity order of magnitude difference in the wall versus in the lumen is between three and nine orders where advection dominates in the lumen while diffusion dominates in the wall (e.g., Figure 4). While transient behavior may alter the luminal advection at the local scale (e.g., Chapter 2 in Durka et al. [71]), such as locations of velocity jet impingement, the coupling between these two regimes is expected to be sufficiently weak that qualitative information (e.g., locations of local maxima/minima) is preserved. The steady flow approximation provides a reasonable solution considering that the calculated Schmidt number is 2100 [72], while significantly reduces the computational costs. In prior studies it has been shown that unsteady flow does not strongly affect the lumen oxygen flux and flow-driven mass transport [73,74]. In regard to the rigid treatment of the artery walls in this work, it is worth noting that the mass boundary layer has a Schmidt number on the order of thousands [58]; implying the mass boundary layer thickness is on the order of 1/1000 the momentum boundary layer thickness. This distance would not be of negligible size with respect to the wall displacement of a healthy artery due to the pulsatile blood flow. It is expected however that luminal wall displacement of the rigid ILT would be substantially less than of a healthy elastic artery wall, and that a zero-velocity boundary condition on the ILT-lumen interface is an appropriate approximation given the aim of the current study. Additionally, if wall elasticity were to be considered, its impacts on the mass boundary layer would be dependent on the tissue properties which can vary among patients. Given the general difficulty in the availability of this data, understanding the sensitivity of this relationship will be the subject of future work. A further limitation in the current study is that the arterial wall oxygen consumption rate has been found to vary spatially as well [60], however, such an experimental study is outside the scope of the present work, and furthermore, is a patient-specific matter. We also note that the geometries considered in this study do not contain a bifurcation. Despite these assumptions, the trend between oxygen transport in AAA and D_{ilt} , K_{ilt} , has been elucidated, keeping all other parameters fixed, in that including the multilayer structure in the ILT does not substantially alter the luminal wall oxygen profile. None of these assumptions would invalidate the conclusions of this study.

Author Contributions: Conceptualization: R.Z., M.B., M.D.; methodology and design of numerical simulations: A.T., R.Z.; data collection, and visualization: A.T., D.B.; analysis and interpretation: R.Z., A.T.; writing—original draft preparation: R.Z., A.T., D.B.; writing—review and editing: R.Z., M.B., A.T.; project administration, supervision, and overall responsibility: R.Z. All authors have read and agreed to the published version of the manuscript.

Funding: R.Z. and A.T. are partially supported by the Samuel and Emma Winters Foundation, Hunkele Dreaded Disease Award, and NSF under grant CBET 2138225. MB is partially supported by the NSF under grants DMS 1912908, DCSD 1934300, DMS 2208219, and DMS 2205695.

Institutional Review Board Statement: Not applicable.

Informed Consent Statement: Not applicable.

Data Availability Statement: All of the data is contained within the article.

Conflicts of Interest: The authors declare no conflict of interest. The funders had no role in the design of the study; in the collection, analyses, or interpretation of data; in the writing of the manuscript, or in the decision to publish the results.

References

1. Jana, S.; Hu, M.; Shen, M.; Kassiri, Z. Extracellular matrix, regional heterogeneity of the aorta, and aortic aneurysm. *Exp. Mol. Med.* **2019**, *51*, 1–15. [CrossRef] [PubMed]

- 2. Kühnl, A.; Erk, A.; Trenner, M.; Salvermoser, M.; Schmid, V.; Eckstein, H.-H. Incidence, treatment and mortality in patients with abdominal aortic aneurysms: An analysis of hospital discharge data from 2005–2014. *Dtsch. Ärzteblatt Int.* **2017**, *114*, 391.
- 3. Kuivaniemi, H.; Ryer, E.J.; Elmore, J.R.; Tromp, G. Understanding the pathogenesis of abdominal aortic aneurysms. *Expert Rev. Cardiovasc. Ther.* **2015**, *13*, 975–987. [CrossRef] [PubMed]
- 4. Sakalihasan, N.; Michel, J.-B.; Katsargyris, A.; Kuivaniemi, H.; Defraigne, J.-O.; Nchimi, A.; Powell, J.T.; Yoshimura, K.; Hultgren, R. Abdominal aortic aneurysms. *Nat. Rev. Dis. Prim.* **2018**, *4*, 34. [CrossRef] [PubMed]
- Grøndal, N.; Søgaard, R.; Lindholt, J. Baseline prevalence of abdominal aortic aneurysm, peripheral arterial disease and hypertension in men aged 65–74 years from a population screening study (VIVA trial). J. Br. Surg. 2015, 102, 902–906. [CrossRef]
- 6. Oliver-Williams, C.; Sweeting, M.; Turton, G.; Parkin, D.; Cooper, D.; Rodd, C.; Thompson, S.; Earnshaw, J. Lessons learned about prevalence and growth rates of abdominal aortic aneurysms from a 25-year ultrasound population screening programme. *J. Br. Surg.* **2018**, *105*, 68–74. [CrossRef]
- 7. Aggarwal, S.; Qamar, A.; Sharma, V.; Sharma, A. Abdominal aortic aneurysm: A comprehensive review. *Exp. Clin. Cardiol.* **2011**, 16, 11–15.
- 8. Li, X.; Zhao, G.; Zhang, J.; Duan, Z.; Xin, S. Prevalence and trends of the abdominal aortic aneurysms epidemic in general population-a meta-analysis. *PLoS ONE* **2013**, *8*, e81260. [CrossRef]
- 9. Harter, L.P.; Gross, B.H.; Callen, P.W.; Barth, R.A. Ultrasonic evaluation of abdominal aortic thrombus. *J. Ultrasound Med.* **1982**, 1, 315–318. [CrossRef]
- 10. Tong, J.; Holzapfel, G.A. Structure, mechanics, and histology of intraluminal thrombi in abdominal aortic aneurysms. *Ann. Biomed. Eng.* **2015**, *43*, 1488–1501. [CrossRef]
- 11. Adolph, R.; Vorp, D.A.; Steed, D.L.; Webster, M.W.; Kameneva, M.V.; Watkins, S.C. Cellular content and permeability of intraluminal thrombus in abdominal aortic aneurysm. *J. Vasc. Surg.* **1997**, 25, 916–926. [CrossRef]
- 12. van Dam, E.A.; Dams, S.D.; Peters, G.W.; Rutten, M.; Schurink, G.W.H.; Buth, J.; van de Vosse, F.N. Determination of linear viscoelastic behavior of abdominal aortic aneurysm thrombus. *Biorheology* **2006**, *43*, 695–707. [PubMed]
- 13. Wilson, J.S.; Virag, L.; Di Achille, P.; Karsaj, I.; Humphrey, J.D. Biochemomechanics of intraluminal thrombus in abdominal aortic aneurysms. *J. Biomech. Eng.* **2013**, *135*, 021011. [CrossRef] [PubMed]
- 14. Matusik, P.; Mazur, P.; Stępień, E.; Pfitzner, R.; Sadowski, J.; Undas, A. Architecture of intraluminal thrombus removed from abdominal aortic aneurysm. *J. Thromb. Thrombolysis* **2010**, *30*, 7–9. [CrossRef] [PubMed]
- 15. Boyd, A.J. Intraluminal thrombus: Innocent bystander or factor in abdominal aortic aneurysm pathogenesis? *JVS Vasc. Sci.* **2021**, 2, 159–169. [CrossRef]
- 16. Hossack, M.; Fisher, R.; Torella, F.; Madine, J.; Field, M.; Akhtar, R. Micromechanical and Ultrastructural Properties of Abdominal Aortic Aneurysms. *Artery Res.* **2022**, *28*, 15–30. [CrossRef]
- 17. Wang, D.H.; Makaroun, M.; Webster, M.W.; Vorp, D.A. Mechanical properties and microstructure of intraluminal thrombus from abdominal aortic aneurysm. *J. Biomech. Eng.* **2001**, *123*, 536–539. [CrossRef]
- 18. Gasser, T.C.; Görgülü, G.; Folkesson, M.; Swedenborg, J. Failure properties of intraluminal thrombus in abdominal aortic aneurysm under static and pulsating mechanical loads. *J. Vasc. Surg.* **2008**, *48*, 179–188. [CrossRef]
- 19. Di Martino, E.S.; Vorp, D.A. Effect of variation in intraluminal thrombus constitutive properties on abdominal aortic aneurysm wall stress. *Ann. Biomed. Eng.* **2003**, *31*, 804–809. [CrossRef]
- 20. Mower, W.R.; Quiñones, W.J.; Gambhir, S.S. Effect of intraluminal thrombus on abdominal aortic aneurysm wall stress. *J. Vasc. Surg.* 1997, 26, 602–608. [CrossRef]
- 21. Wang, D.H.; Makaroun, M.S.; Webster, M.W.; Vorp, D.A. Effect of intraluminal thrombus on wall stress in patient-specific models of abdominal aortic aneurysm. *J. Vasc. Surg.* **2002**, *36*, 598–604. [CrossRef]
- 22. Li, Z.Y.; U-King-Im, J.; Tang, T.Y.; Soh, E.; See, T.C.; Gillard, J.H. Impact of calcification and intraluminal thrombus on the computed wall stresses of abdominal aortic aneurysm. *J. Vasc. Surg.* **2008**, *47*, 928–935. [CrossRef]
- 23. Haller, S.J.; Crawford, J.D.; Courchaine, K.M.; Bohannan, C.J.; Landry, G.J.; Moneta, G.L.; Azarbal, A.F.; Rugonyi, S. Intraluminal thrombus is associated with early rupture of abdominal aortic aneurysm. *J. Vasc. Surg.* **2018**, *67*, 1051–1058.e1. [CrossRef]
- 24. Bluestein, D.; Dumont, K.; De Beule, M.; Ricotta, J.; Impellizzeri, P.; Verhegghe, B.; Verdonck, P. Intraluminal thrombus and risk of rupture in patient specific abdominal aortic aneurysm—FSI modelling. *Comput. Methods Biomech. Biomed. Eng.* **2009**, 12, 73–81. [CrossRef]
- 25. Piechota-Polanczyk, A.; Jozkowicz, A.; Nowak, W.; Eilenberg, W.; Neumayer, C.; Malinski, T.; Huk, I.; Brostjan, C. The abdominal aortic aneurysm and intraluminal thrombus: Current concepts of development and treatment. *Front. Cardiovasc. Med.* **2015**, 2, 19. [CrossRef]
- 26. Vorp, D.A.; Lee, P.C.; Wang, D.H.; Makaroun, M.S.; Nemoto, E.M.; Ogawa, S.; Webster, M.W. Association of intraluminal thrombus in abdominal aortic aneurysm with local hypoxia and wall weakening. *J. Vasc. Surg.* **2001**, *34*, 291–299. [CrossRef]
- 27. Vorp, D.; Wang, D.; Webster, M.; Federspiel, W. Effect of intraluminal thrombus thickness and bulge diameter on the oxygen diffusion in abdominal aortic aneurysm. *J. Biomech. Eng.* **1998**, *120*, 579–583. [CrossRef]

28. Heistad, D.D.; Marcus, M.L.; Larsen, G.E.; Armstrong, M.L. Role of vasa vasorum in nourishment of the aortic wall. *Am. J. Physiol.-Heart Circ. Physiol.* **1981**, 240, H781–H787. [CrossRef]

- 29. Herrmann, J.; Lerman, L.O.; Rodriguez-Porcel, M.; Holmes, D.R., Jr.; Richardson, D.M.; Ritman, E.L.; Lerman, A. Coronary vasa vasorum neovascularization precedes epicardial endothelial dysfunction in experimental hypercholesterolemia. *Cardiovasc. Res.* **2001**, *51*, 762–766. [CrossRef]
- Vorp, D.A.; Geest, J.P.V. Biomechanical determinants of abdominal aortic aneurysm rupture. Arterioscler. Thromb. Vasc. Biol. 2005, 25, 1558–1566. [CrossRef]
- 31. Salman, H.E.; Ramazanli, B.; Yavuz, M.M.; Yalcin, H.C. Biomechanical Investigation of Disturbed Hemodynamics-Induced Tissue Degeneration in Abdominal Aortic Aneurysms Using Computational and Experimental Techniques. *Front. Bioeng. Biotechnol.* **2019**, 7, 111. [CrossRef] [PubMed]
- 32. Yunoki, K.; Naruko, T.; Sugioka, K.; Inaba, M.; Iwasa, Y.; Komatsu, R.; Itoh, A.; Haze, K.; Inoue, T.; Yoshiyama, M. Erythrocyte-rich thrombus aspirated from patients with ST-elevation myocardial infarction: Association with oxidative stress and its impact on myocardial reperfusion. *Eur. Heart J.* 2012, 33, 1480–1490. [CrossRef] [PubMed]
- 33. Meyer, C.A.; Guivier-Curien, C.; Moore, J.E., Jr. Trans-thrombus blood pressure effects in abdominal aortic aneurysms. *J. Biomech. Eng.* **2010**, *1*32, 071005. [CrossRef] [PubMed]
- 34. Zakerzadeh, R.; Zunino, P. A computational framework for fluid–porous structure interaction with large structural deformation. *Meccanica* **2019**, *54*, 101–121. [CrossRef]
- 35. Zakerzadeh, R. A Computational Model for Fluid-Porous Structure Interaction. Ph.D. Thesis, University Of Pittsburgh, Pttsburgh, PA, USA, 2016.
- 36. Zakerzadeh, R.; Bukac, M.; Zunino, P. Computational analysis of energy distribution of coupled blood flow and arterial deformation. *Int. J. Adv. Eng. Sci. Appl. Math.* **2015**, *8*, 70–85. [CrossRef]
- 37. Koshiba, N.; Ando, J.; Chen, X.; Hisada, T. Multiphysics simulation of blood flow and LDL transport in a porohyperelastic arterial wall model. *J. Biomech. Eng.* **2007**, 129, 374–385. [CrossRef]
- 38. Simon, B.R.; Gaballa, M.A. Finite Strain, Poroelastic Finite Element Models for Large Arterial Cross Sections. *Comput. Methods Bioeng.* **1988**, *9*, 325–334.
- 39. Du, J.; Kim, D.; Alhawael, G.; Ku, D.N.; Fogelson, A.L. Clot permeability, agonist transport, and platelet binding kinetics in arterial thrombosis. *Biophys. J.* **2020**, *119*, 2102–2115. [CrossRef]
- 40. Raptis, A.; Xenos, M.; Dimas, S.; Giannoukas, A.; Labropoulos, N.; Bluestein, D.; Matsagkas, M.I. Effect of macroscale formation of intraluminal thrombus on blood flow in abdominal aortic aneurysms. *Comput. Methods Biomech. Biomed. Eng.* **2016**, *19*, 84–92. [CrossRef]
- 41. Polzer, S.; Gasser, T.C.; Markert, B.; Bursa, J.; Skacel, P. Impact of poroelasticity of intraluminal thrombus on wall stress of abdominal aortic aneurysms. *Biomed. Eng. Online* **2012**, *11*, 62. [CrossRef]
- 42. Ayyalasomayajula, A.; Vande Geest, J.P.; Simon, B.R. Porohyperelastic finite element modeling of abdominal aortic aneurysms. *J. Biomech. Eng.* **2010**, 132, 104502. [CrossRef]
- 43. Carbino, B.; Guy, A.; Durka, M.; Zakerzadeh, R. The Effects of Geometric Features of Intraluminal Thrombus on the Vessel Wall Oxygen Deprivation. *Front. Bioeng. Biotechnol.* **2022**, *10*, 814995. [CrossRef]
- 44. Toungara, M.; Geindreau, C. Influence of a poro-mechanical modeling of the intra-luminal thrombus and the anisotropy of the arterial wall on the prediction of the abdominal aortic aneurysm rupture. *Cardiovasc. Eng. Technol.* **2013**, *4*, 192–208. [CrossRef]
- 45. Bukač, M.; Shadden, S.C. Quantifying the effects of intraluminal thrombi and their poroelastic properties on abdominal aortic aneurysms. *Arch. Appl. Mech.* **2021**, *92*, 435–446. [CrossRef]
- 46. Sun, N.; Leung, J.H.; Wood, N.B.; Hughes, A.D.; Thom, S.A.; Cheshire, N.J.; Xu, X.Y. Computational analysis of oxygen transport in a patient-specific model of abdominal aortic aneurysm with intraluminal thrombus. *Br. J. Radiol.* **2009**, *82*, S18–S23. [CrossRef] [PubMed]
- 47. Loffredo, S.; Guivier-Curien, C.; Deplano, V. Influence of the presence of a porous thrombus on hemodynamics in a CFD model of a descending thoracic aneurysm. In Proceedings of the Congrès de la Société de Biomécanique, St. Etienne, France, 25–27 October 2021; Informa UK Limited: Colchester, UK, 2021; pp. S189–S191.
- 48. Zakerzadeh, R.; Cupac, T.; Durka, M. Oxygen transport in a permeable model of abdominal aortic aneurysm. *Comput. Methods Biomech. Biomed. Eng.* **2020**, 24, 215–229. [CrossRef]
- 49. Zakerzadeh, R.; Cupac, T.; Dorfner, N.; Guy, A. Coupled Hemodynamics and Oxygen Diffusion in Abdominal Aortic Aneurysm: A Computational Sensitivity Study. *Cardiovasc. Eng. Technol.* **2021**, *12*, 166–182. [CrossRef]
- 50. Throop, A.; Bukac, M.; Zakerzadeh, R. Prediction of wall stress and oxygen flow in patient-specific abdominal aortic aneurysms: The role of intraluminal thrombus. *Biomech. Model. Mechanobiol.* **2022**, 1–19. [CrossRef]
- 51. Scotti, C.M.; Shkolnik, A.D.; Muluk, S.C.; Finol, E.A. Fluid-structure interaction in abdominal aortic aneurysms: Effects of asymmetry and wall thickness. *Biomed. Eng. Online* **2005**, *4*, 64. [CrossRef]
- 52. Hirsch, A.T.; Haskal, Z.J.; Hertzer, N.R.; Bakal, C.W.; Creager, M.A.; Halperin, J.L.; Hiratzka, L.F.; Murphy, W.R.; Olin, J.W.; Puschett, J.B. ACC/AHA 2005 practice guidelines for the management of patients with peripheral arterial disease (lower extremity, renal, mesenteric, and abdominal aortic). *Circulation* **2006**, *113*, e463–e654. [CrossRef]
- 53. Cnotliwy, M.; Kolasa, A.; Kwas, A.; Kazimierczak, A.; Wiernicki, I. C-Reactive Protein within the Wall of Large Abdominal Aortic Aneurysms; Pathophysiological Implications. A Preliminary Study. *Pol. J. Surg.* **2010**, *82*, 193–198. [CrossRef]

54. Martufi, G.; Satriano, A.; Moore, R.D.; Vorp, D.A.; Martino, E.S.D. Local Quantification of Wall Thickness and Intraluminal Thrombus Offer Insight into the Mechanical Properties of the Aneurysmal Aorta. *Ann. Biomed. Eng.* **2014**, *43*, 1759–1771. [CrossRef] [PubMed]

- 55. Rappitsch, G.; Perktold, K. Computer simulation of convective diffusion processes in large arteries. *J. Biomech.* **1996**, 29, 207–215. [CrossRef]
- 56. Ku, D.N. Blood flow in arteries. Annu. Rev. Fluid Mech. 1997, 29, 399–434. [CrossRef]
- 57. Kemmerling, E.M.C.; Peattie, R.A. Abdominal Aortic Aneurysm Pathomechanics: Current Understanding and Future Directions. *Adv. Exp. Med. Biol.* **2018**, *1097*, 157–179.
- 58. Moore, J.A.; Ethier, C.R. Oxygen mass transfer calculations in large arteries. J. Biomech. Eng. 1997, 119, 469–475. [CrossRef]
- 59. Iannetti, L.; D'Urso, G.; Conoscenti, G.; Cutri, E.; Tuan, R.S.; Raimondi, M.T.; Gottardi, R.; Zunino, P. Distributed and Lumped Parameter Models for the Characterization of High Throughput Bioreactors. *PLoS ONE* **2016**, *11*, e0162774. [CrossRef]
- 60. Buerk, D.G.; Goldstick, T.K. Arterial wall oxygen consumption rate varies spatially. *Am. J. Physiol.-Heart Circ. Physiol.* **1982**, 243, H948–H958. [CrossRef]
- 61. Fang, Q.; Sakadžić, S.; Ruvinskaya, L.; Devor, A.; Dale, A.M.; Boas, D.A. Oxygen advection and diffusion in a three-dimensional vascular anatomical network. *Opt. Express* **2008**, *16*, 17530–17541. [CrossRef]
- 62. Lücker, A.; Weber, B.; Jenny, P. A dynamic model of oxygen transport from capillaries to tissue with moving red blood cells. *Am. J. Physiol.-Heart Circ. Physiol.* **2015**, 308, H206–H216. [CrossRef]
- 63. Muthard, R.W.; Diamond, S.L. Blood clots are rapidly assembled hemodynamic sensors: Flow arrest triggers intraluminal thrombus contraction. *Arterioscler. Thromb. Vasc. Biol.* **2012**, *32*, 2938–2945. [CrossRef] [PubMed]
- 64. Brass, L.F.; Wannemacher, K.M.; Ma, P.; Stalker, T.J. Regulating thrombus growth and stability to achieve an optimal response to injury. *J. Thromb. Haemost.* **2011**, *9*, 66–75. [CrossRef] [PubMed]
- 65. Fraser, K.H.; Meagher, S.; Blake, J.R.; Easson, W.J.; Hoskins, P.R. Characterization of an abdominal aortic velocity waveform in patients with abdominal aortic aneurysm. *Ultrasound Med. Biol.* **2008**, *34*, 73–80. [CrossRef]
- 66. Applegate, R.L., II; Dorotta, I.L.; Wells, B.; Juma, D.; Applegate, P.M. The relationship between oxygen reserve index and arterial partial pressure of oxygen during surgery. *Anesth. Analg.* **2016**, 123, 626. [CrossRef] [PubMed]
- 67. Buerk, D.G.; Goldstick, T.K. Oxygen tension changes in the outer vascular wall supplied by vasa vasorum following adenosine and epinephrine. *J. Vasc. Res.* **1986**, 23, 9–21. [CrossRef]
- 68. Vosse, F.N.v.d.; Stergiopulos, N. Pulse Wave Propagation in the Arterial Tree. Annu. Rev. Fluid Mech. 2011, 43, 467–499. [CrossRef]
- 69. Reymond, P.; Merenda, F.; Perren, F.; Rufenacht, D.; Stergiopulos, N. Validation of a one-dimensional model of the systemic arterial tree. *Am. J. Physiol.-Heart Circ. Physiol.* **2009**, 297, H208–H222. [CrossRef]
- 70. Perktold, K.; Prosi, M.; Zunino, P. Mathematical models of mass transfer in the vascular walls. In *Cardiovascular Mathematics: Modeling and Simulation of the Circulatory System*; Formaggia, L., Quarteroni, A., Veneziani, A., Eds.; Springer: Milano, Italy, 2009; pp. 243–278.
- 71. Durka, M.J. A Numerical Investigation into the Hemodynamics Oxygen Transport and Flow Stability of Cerebral Aneurysms. Ph.D. Thesis, University of Pittsburgh, Pittsburgh, PA, USA, 2020.
- 72. Ma, P.; Li, X.; Ku, D.N. Heat and mass transfer in a separated flow region for high Prandtl and Schmidt numbers under pulsatile conditions. *Int. J. Heat Mass Transf.* **1994**, *37*, 2723–2736. [CrossRef]
- 73. Kolandavel, M.K.; Fruend, E.T.; Ringgaard, S.; Walker, P.G. The effects of time varying curvature on species transport in coronary arteries. *Ann. Biomed. Eng.* **2006**, *34*, 1820–1832. [CrossRef]
- 74. Liu, X.; Fan, Y.; Deng, X.; Zhan, F. Effect of non-Newtonian and pulsatile blood flow on mass transport in the human aorta. *J. Biomech.* **2011**, *44*, 1123–1131. [CrossRef]